PNAS
www.pnas.org

Supplementary Information for

Two-step crystallization and solid-solid transitions in binary colloidal mixtures

Huang Fang, Michael F. Hagan, W. Benjamin Rogers

W. Benjamin Rogers
E-mail: wrogers@brandeis.edu

This PDF file includes:

Supplementary text
Figs. S1 to S12
Tables S1 to S2
Legends for Movies S1 to S6
SI References

Other supplementary materials for this manuscript include the following:

Movies S1 to S6

Supporting Information Text

Particle Synthesis. We synthesize DNA-grafted colloidal particles following a modified version of the method described in Ref (1). In brief, the method is comprised of three steps: 1) Azide groups are attached to the ends of polystyrene-poly(ethylene oxide) (PS-PEO) diblock copolymers; 2) The azide-modified PS-PEO copolymers are physically grafted to the surface of polystyrene colloids; and 3) Single-stranded DNA molecules are conjugated to the ends of the grafted PS-PEO copolymers by strain-promoted click chemistry. The specific protocol we use is described below.

We make azide-modified PS-PEO by first functionalizing PS-PEO with chlorine groups and then substituting the chlorine groups with azide groups. To obtain PS-PEO-Cl, we mix 100 mg of PS-PEO, 2 ml of dichloromethane, and 42 μl of triethylamine in a glass vial, and stir the mixture for 15 minutes on ice. Next we add 23.5 μl of methanesulfonyl chloride, stir the solution on ice for 2 hours, remove it from the ice bath and stir at room temperature for 22 hours. After the reaction, we dry the solution and wash the dried pellet twice with a mixture of 10 ml anhydrous methanol (MeOH) and 243 μl of 37 % hydrochloric acid and then twice with a solution of 3 ml of MeOH and 40 ml of diethyl ether. In each washing step, we dissolve the pellet and then precipitate the PS-PEO by placing the sample in the freezer for one hour. Then we centrifuge the solution at 4500 rpm at 2 °C for 10 minutes to form a pellet and pour off the supernatant. After washing, we dry the pellet again.

Next we substitute the chlorine groups with azide groups. Specifically, we mix 10 mg of sodium azide, 2 ml of dimethylformamide, and the dried PS-PEO pellet. We place the solution in a 65 °C oil bath and stir at 1500 rpm for 24 hours. After the reaction, we wash the mixture with 40 ml of diethyl ether and then with a solution containing 3 ml of MeOH and 40 ml of diethyl ether three times. We use the same washing procedure as we previously described. Then we dry the pellet and resuspend the dried PS-PEO-N_3 pellet in deionized (DI) water to a concentration of 100 mM.

We attach the azide-modified PS-PEO copolymer to the surface of polystyrene colloids using a physical grafting method. We first adsorb PS-PEO-N_3 to the surface of polystyrene colloids by mixing 160 μl of 100 mM PS-PEO-N_3, 160 μl of tetrahydrofuran, 40 μl of deionized (DI) water, and 40 μl of 10 %(v/v) 600-nm-diameter PS particles (Molecular Probes), and then vortex the mixture for 30 minutes. Next, we dilute the mixture 10x with DI water, wash the particles with DI water five times, and concentrate the particles back to 1 %(v/v) after washing.

We dye particles with different fluorophores so that we can distinguish between different particle species. Specifically, we label two types of particles, one with nile red and the other with pyrromethene green. We first make saturated solutions of fluorescent dye dissolved in toluene. We mix 4 μl of 10 % saturated nile red or 50 % saturated perromethene green in toluene and 400 μl 1 % azide-functionalized PS particles and rotate end-over-end for 7 hours. Next we open the sample to air and heat in an oven at 90 °C for 12 minutes. After that, we wash the dyed particles five times in DI water by centrifugation and resuspension.

Finally we attach DNA molecules to the azide-modified PS-PEO copolymers using strain-promoted click chemistry. We mix 40 μl of 1 % azide-functioned PS particles, 10 μl of 100 μM ssDNA, and 150 μl 1XTE/1 M NaCl buffer, and heat the sample in an oven at 70 °C for 24 hours. For particle A, we add 10 μl of sequence S; for particle B with mixing ratio α, we add 10α μl of S and $10(1-\alpha)$ μl of S^*. After the reaction, we wash the DNA-coated particles with DI water five times by centrifugation and resuspension. The DNA sequences (Integrated DNA Technologies) we use are:

S 5'-DBCO-$(T)_{51}$-GA GTT GCG GTA GAC-3'
S^* 5'-DBCO-$(T)_{51}$-AA TGC CTG TCT ACC-3'

Crystallization Experiments. We physically constrain the particles between two plasma-cleaned glass coverslips to create a two-dimensional suspension and crystallize the particles *in situ* on an optical microscope.

We seal the binary colloidal suspension in a two-dimensional sample chamber. We mix 1 μl of 2 %(v/v) DNA-coated particle A, 1 μl of 2 %(v/v) DNA-coated particle B and 2 μl of 1XTE Buffer with 500 mM NaCl. We take 1 μl of the solution and pipette it onto a plasma-cleaned 24 mm×60 mm coverslip. Then we cover the liquid with a 15 mm×15 mm plasma-cleaned coverslip and squeeze the two coverslips together to make the spacing between the coverslips comparable to the particles' diameter. Finally, we seal the sample chamber with UV glue to prevent leakage or evaporation.

Next, we crystallize the sample on an optical microscope and record videos of the crystallization pathways and equilibrium crystal structures. We place the sample chamber on the microscope stage and mount a homemade heating block on top of the sample, which can be controlled via a PID controller with a GUI interface. We begin every crystallization experiment by first raising the temperature to completely melt the sample. Then we roughly find the melting temperature of the sample, defined as the temperature at which 50% of particles are unbound. After remelting the sample again, we quench and hold the temperature roughly ∼0.3 °C above the melting temperature and record a video of crystallization, which takes around one hour to obtain large 2D crystalline domains. We use a Nikon Eclipse Ti2 and CoolSNAP HQ2 CCD camera to take bright-field videos of crystallization, and a Leica SP8 to take confocal fluorescence images of 2D crystalline domains. See Movies S1, S2, and S3 for representative examples of crystallization.

Image Processing and Analysis. We use ImageJ to analyze our confocal fluorescence images. Fig. S1 shows examples of raw images taken using the confocal microscope. In the main text, we show zoomed-in, cropped images to highlight the lattice structures and compositions that we observe. However, we observe numerous similar crystals across the sample chamber, with typical domain sizes of roughly 10 μm.

We use freely-available MATLAB routines to find and track all particles in our bright-field microscopy videos (2). Fig. S2 shows the procedure of image processing. First, we find the centroid positions of all particles in each image. Next we identify

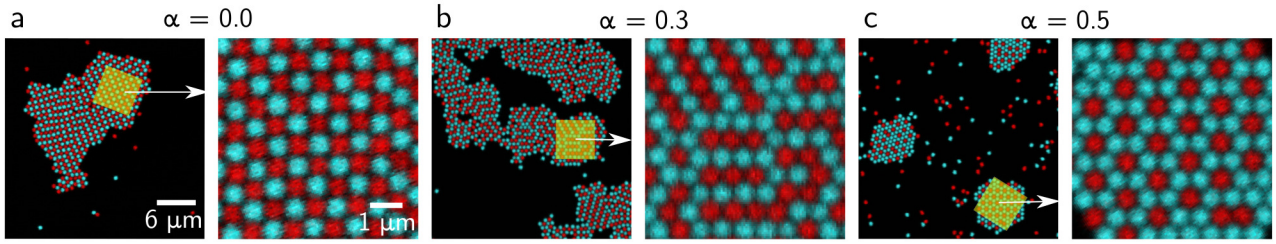

Fig. S1. Raw and cropped images from confocal fluorescence crystallization experiments: (a) α=0.0; (b) α=0.3; and (c)α=0.5. Images on the left show a single field of view; images on the right show the regions of interest highlighted in yellow.

all of the particles that are in the largest cluster using a cutoff radius of 1.1σ, where σ is the particle diameter. Next we compute the local bond orientation order parameter ψ for each particle in the cluster:

$$\psi_m = \frac{1}{N_b}\sum_{N_b} \exp(-im\theta_b) \qquad m = 4, 6 \qquad [1]$$

where m can be either 4 or 6. N_b is the number of nearest neighbors around the specified particle. θ_b is the angle between the bond orientation and a reference axis. The bond orientation is defined by the vector pointing from the center of each particle to the center of its nearest neighbor. Finally, we compute the global order parameter Φ of the largest crystalline domain to distinguish between square and hexagonal lattices. Φ is defined by

$$\Phi = \frac{2}{\pi}\tan^{-1}\left(\frac{\Psi_6}{\Psi_4}\right) \qquad [2]$$

$$\Psi_m = \left|\frac{1}{N_c}\sum_{N_c} \psi_m\right| \qquad m = 4, 6 \qquad [3]$$

where Ψ_4 and Ψ_6 are global bond orientation order parameters, and ψ_4 and ψ_6 are local bond orientation order parameters. N_c is the total number of particles in the cluster. Ψ_m is a measure of m-fold global symmetry. When Ψ_m is close to 1, the measured pattern has m-fold symmetry.

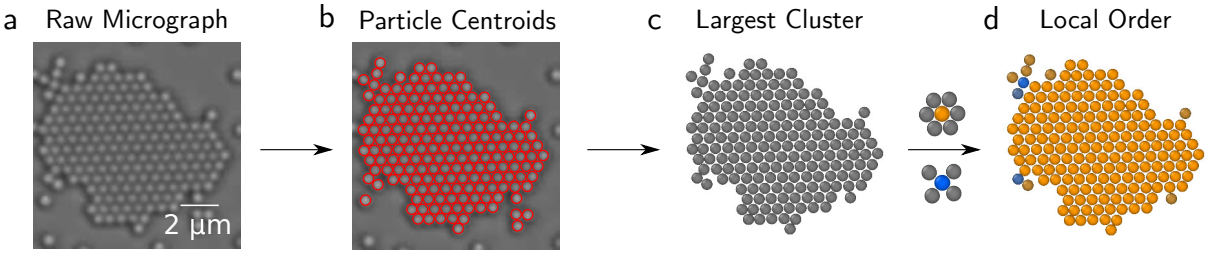

Fig. S2. Analysis of brightfield micrographs. (a) shows a typical micrograph; (b) shows the same micrograph overlaid with the particle centroid positions; (c) shows a rendering of the largest cluster in the frame; and (d) shows the local ordered (color code) of each particle in the cluster: blue indicates square symmetry and orange indicates hexagonal symmetry.

Lattice Constants and Crystal Densities. We measure the lattice constants of different crystal lattices by computing the pair correlation function $g(r)$ of single-crystal domains. More specifically, we compute $g(r)$ from a brightfield micrograph of a single crystal of bare polystyrene particles formed by drying a dilute suspension on a cleaned glass coverslip (Fig. S3a). We also compute $g(r)$ for each of the different self-assembled lattice structures using the confocal fluorescence images shown in Fig. S1 (Fig. S3b–d). The interparticle distance r corresponding to the first peak indicates the separation between nearest neighbors in the lattice structure. Red solid lines show a Gaussian fit to the first peak. We find that the diameter of the bare polystyrene particles is 619 nm. Lattice constants of all structures are also shown in Fig. S3. The nearest-neighbor separations within the self-assembled crystals are roughly 640 nm, which is consistent with the fact that the single-stranded DNA coated on the particle surface is 10–15 nm long.

We compute the area fractions of the checkerboard, stripe, and honeycomb lattices by calculating the mean density within a circular area inside the bulk that includes more than 30 particles. The area fraction of the checkerboard lattice is 76%, while the area fraction of the stripe and honeycomb lattices is 84%. The lower area fraction of the checkerboard lattice further supports the hypothesis that the checkerboard lattice has a higher entropy than the stripe lattice because particles within the checkerboard lattice can explore a larger area within their lattice sites, as compared to particles within the stripe lattice.

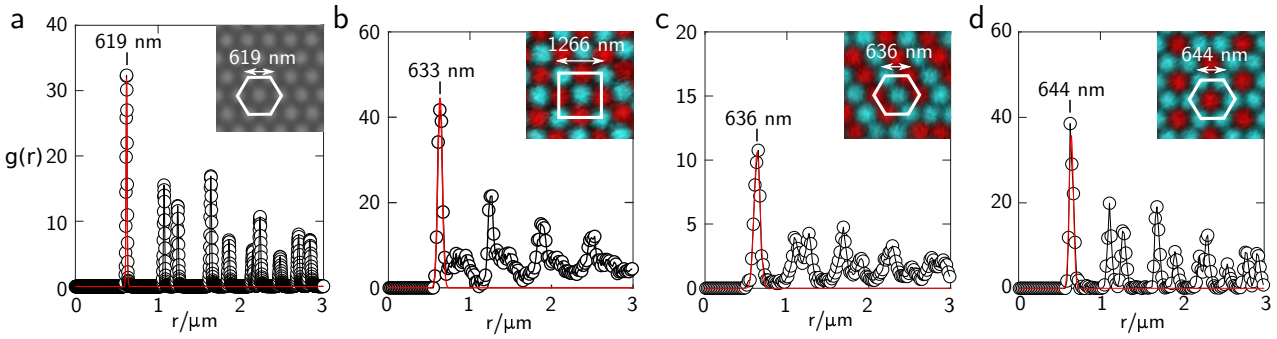

Fig. S3. The pair correlation functions $g(r)$ for different lattice structures identify the lattice constants. (a) $g(r)$ measured from a bright-field micrograph of bare polystyrene particles; (b) $g(r)$ measured for the checkerboard lattice; (c) $g(r)$ measured for the stripe lattice; and (d) $g(r)$ measured for the honeycomb lattice. Red solid lines show Gaussian fits to the first peak of $g(r)$. The first peak of $g(r)$ corresponds to the mode of the distance between nearest neighbors. Insets show micrographs of the corresponding crystal lattices.

Lattice Rigidity. We observe that the checkerboard lattice is floppier than the stripe lattice in experiments. Fig. S4 shows the distribution of the magnitudes of displacements of particles within a single crystallite within a one-second time span. The histogram is made from 50 consecutive snapshots following crystal growth. The two snapshots show representative crystal types and the yellow arrows show the magnitude and direction of one-second displacements. The length of the arrow is proportional to the magnitude of the displacement. The comparison is made between crystals with similar sizes. We observe that the displacement distribution for the checkerboard crystal is much broader than the distribution for the stripe crystal, and has a larger mean value. We also notice that the displacement of particles near the crystal surface is larger than inside the bulk for the checkerboard crystal, which is consistent with the notion that the checkerboard lattice has a lower effective surface free energy. Furthermore, the checkerboard crystals also often have very irregular interfaces.

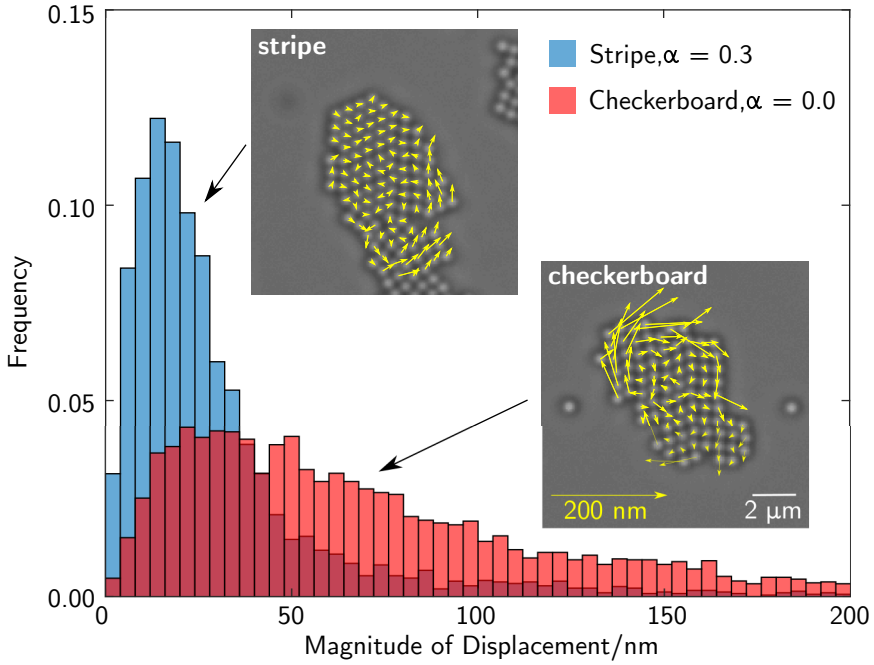

Fig. S4. Checkerboard crystals are floppier than stripe crystals. The histograms show the magnitudes of displacements of particles during one second within two crystal symmetries: a checkerboard crystal (red) and a stripe crystal (blue). The statistics are collected from 50 consecutive snapshots with one-second time intervals. Micrographs show snapshots of the two crystal lattices. Yellow arrows represent the displacement of each particle during a one second interval.

Grand Canonical Monte Carlo Simulations. We use an in-house code written in C++ to perform Grand Canonical Monte Carlo (GCMC) simulations. All particles have the same diameter, which we set to a dimensionless value of 1. The stoichiometry N_A:N_B is 1:1. We use periodic boundary conditions with a box size of 53.3×53.3. The pair potential that we employ is obtained from empirical interaction potentials between DNA-coated particles reported in Ref (3). We define the depth of the pair potential as the binding free energy E_{ij}, and interpolate between tabulated potentials to obtain finely-spaced values of the binding free energy. The width of the pair potential is set to roughly 5% of the diameter of the particles.

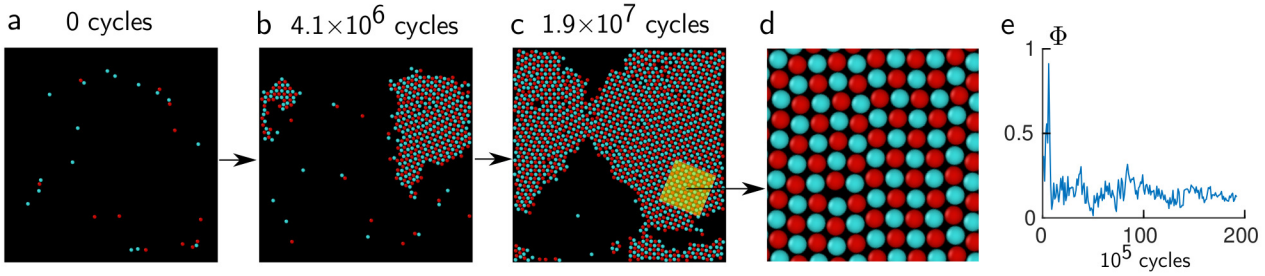

Fig. S5. Snapshots of the whole simulation box at different numbers of Monte Carlo cycles for a grand canonical Monte Carlo simulation for binding strengths $E_{BB} = E_{AA} = 0.0$ and $E_{AB} = 7.1\ k_BT$. (a) 0 cycles; (b) 4.1×10^6 cycles; (c) 1.9×10^7 cycles; (d) Magnified image of the highlighted region in (c). (e) The order parameter Φ as a function of the number of cycles, showing that the simulation has converged according to the criteria discussed in the SI text.

For each simulation, we initialize the system by randomly distributing particles in the simulation box, requiring that no two particles overlap. We set the initial particle area fraction to 0.5%, which corresponds to the same number density as the ideal gas particle reservoir. Then we make displacive moves, insertion/deletion moves, and particle species flipping moves, and determine whether or not to accept these moves using the Metropolis criterion. The x and y displacements of each displacive step are drawn from a uniform distribution with the maximum step length of 0.2. We define one cycle of moves to be equal to 1000 displacive trials. This number is chosen to be equal to roughly the number of particles in a simulation box when filled to 40% by hexagonally-packed particles. The insertion/deletion trials are made with an average frequency of one attempt per cycle. To facilitate equilibration, particularly with regard to compositional order, we make particle species flipping trials in which the species of one randomly-chosen particle is flipped, also with an average frequency of one trial per cycle. Finally, we save particle coordinates every 10^5 cycles.

We perform simulations for at least 10^7 cycles to ensure that the system converges to its equilibrium distribution. To monitor the extent of equilibration after 10^7 cycles, we measure the global order parameter Φ (Eq.(1) of the main text) for the largest crystalline domain in the system, and compute its mean and standard deviation over a window of 5×10^5 consecutive cycles (Fig. S5). If both the mean value and standard deviation vary by less than 0.05 within this window, we specify the simulation as equilibrated and stop the run. Then we analyze these last 5×10^5 cycles to determine the equilibrium state based on the average order parameter. We note that 5×10^5 cycles is much longer than the span needed for a nucleus to grow beyond the critical size, which takes less than 10^3 cycles. Further validations show that other macroscopic properties, such as stoichiometry and compositional order, are also constant after equilibration. We perform one simulation for most of the binding strengths shown on the phase diagram. To validate our results, we do multiple simulations for a few binding free energies for each crystal phase. These repeats generate the same crystal symmetry, stoichiometry, compositional order and other macroscopic properties. See Fig. S5 and Movies S4, S5, S6 for examples of GCMC simulations.

Determination of Crystal Phases. We identify crystalline domains by analyzing the nearest neighbors and local order of each particle in the largest crystalline domain. We compute the complex local bond orientation order parameter ψ_4 and ψ_6 of each particle. If both $|\psi_4|$ and $|\psi_6|$ are smaller than 0.4, then the particle is identified as disordered. Otherwise, if $|\psi_6|$ is closer to 1, then the particle is identified to have hexagonal order. If $|\psi_4|$ is closer to 1, then the particle is identified to have square order. We define a crystal as a set of continuously connected particles with consistent local order and bond orientation. The bond orientation is characterized by the orientation of the complex order parameter ψ_4 or ψ_6, namely $\arg(\psi_m)$. The index m can be either 4 or 6 based on the crystalline symmetry. Particles are considered to have the same orientation if the difference of $\arg\psi$ between neighboring particles is less than $\pi/20$. Particles with nearest-neighbor distances less than 1.1σ are connected, where σ is the particle diameter.

We compute the global order parameter Φ of the largest crystalline domain to distinguish between square and hexagonal lattices. Φ is defined in the main text and previous section **Image Processing and Analysis**. We determine that $\Phi \gtrsim 0.9$ corresponds to a hexagonal lattice and $\Phi \lesssim 0.5$ corresponds to a square lattice.

Finally, we characterize the compositional order of the hexagonal crystal phases by the fraction of honeycomb-like particles and the stoichiometry N_A:N_B. A honeycomb-like particle is characterized by one A particle surrounded by six B particles. Fig. S6 shows the average honeycomb fraction and the stoichiometry N_A:N_B in crystals with similar sizes (roughly 2300 particles) as a function of E_{BB}/E_{AB}. Areas shaded in orange show the honeycomb-like particles. We find that honeycomb fraction is a nonmonotonic function of the ratio of binding strengths between like and unlike particles, reaching a maximum of $\gtrsim 40\%$ at $E_{BB}/E_{AB} \approx 0.8$. Three snapshots from left to right correspond to stripe, honeycomb and demixed crystal phases. The stoichiometry N_A:N_B decreases from 1 to 0 as E_{BB}/E_{AB} increases. We identify crystals having a honeycomb fraction above 25% as honeycomb crystals. If the honeycomb fraction is less than 25% and stoichiometry N_A:N_B is greater than 0.5, we identify the crystal to be a stripe crystal. If the honeycomb fraction is less than 25% and stoichiometry N_A:N_B is less than 0.5, we identify the crystal as a demixed crystal.

Umbrella Sampling. We use in-house code written in C++ to perform umbrella sampling and code written in MATLAB to compute the free-energy landscapes. We choose binding strengths so that only one crystal nucleates within the simulation box

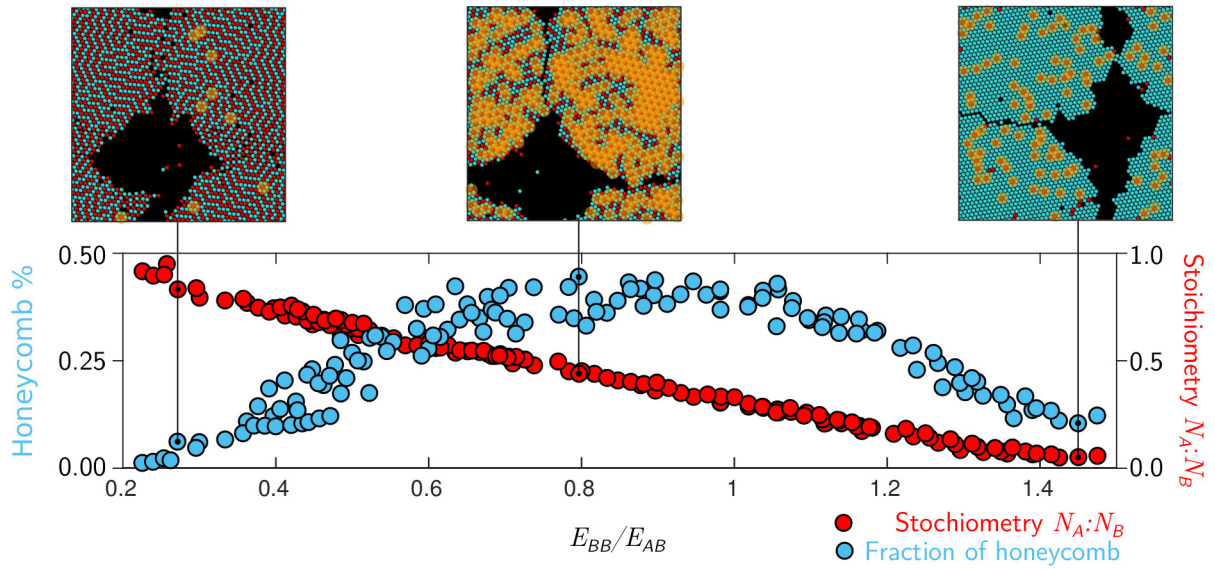

Fig. S6. Identifying the compositional order of hexagonal crystal lattices. The plot shows the fraction of honeycomb phase and stoichiometry N_A:N_B as a function of E_{BB}/E_{AB} near the fluid-crystal boundary. Blue symbols represent the fraction of honeycomb composition; red symbols represent the stoichiometry N_A:N_B for the same set of parameters. Snapshots show representative crystals. The orange regions show domains with honeycomb compositional order. Three snapshots show a stripe crystal (left), a honeycomb crystal (middle), and a demixed crystal (right) composed of ∼2300 particles.

and bias along two progress coordinates: the total number of particles in the biggest cluster N_c and the order parameter Φ of the biggest cluster. The biasing potential that we use is a combination of a harmonic potential with respect to N_c and Φ, and a hard wall potential given by

$$U_{bias}(N_c,\Phi) = \frac{K_N}{2}(N_c - N_c^0)^2 + \frac{K_\Phi}{2}((\Phi - \Phi^0)^2 + U_H \qquad [4]$$

and

$$U_H = \begin{cases} 0 & \sqrt{\Psi_4^2 + \Psi_6^2} > 0.4 \\ \infty & \sqrt{\Psi_4^2 + \Psi_6^2} \leq 0.4. \end{cases}$$

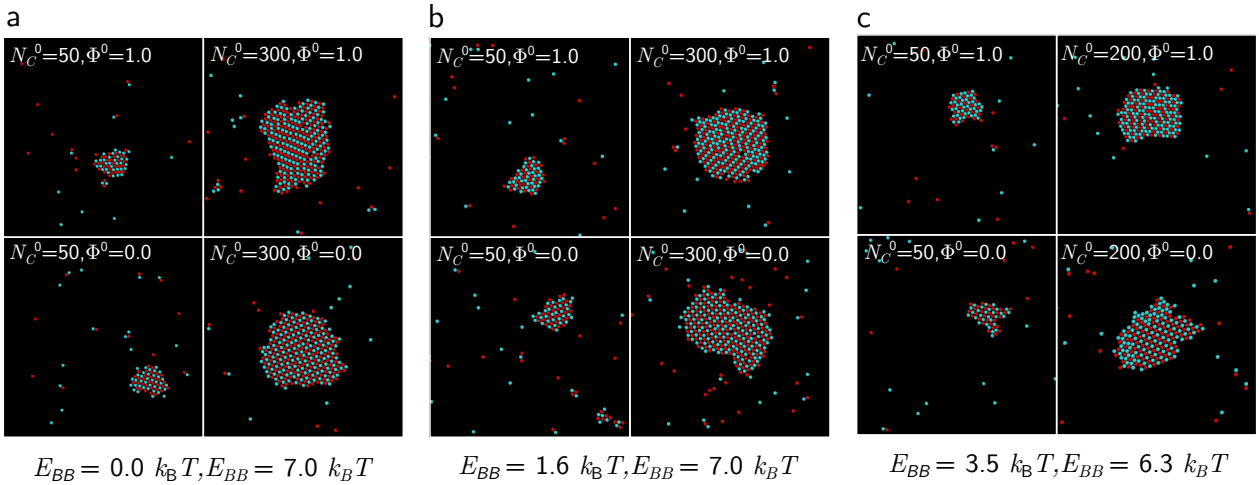

Fig. S7. Snapshots showing the end states of multiple umbrella sampling simulations for different binding strengths. (a) $E_{BB} = 0.0, E_{AB} = 7.0\ k_B T$. The crystal structure is biased between checkerboard and stripe; (b) $E_{BB} = 1.6\ k_B T, E_{AB} = 7.0\ k_B T$. The crystal structure is biased between checkerboard and stripe; (c) $E_{BB} = 3.5\ k_B T, E_{AB} = 6.3\ k_B T$. The crystal structure is biased between checkerboard and honeycomb.

The hard wall potential U_H guarantees that the simulation evolves such that the crystalline lattice remains ordered. If Ψ_4 and Ψ_6 are simultaneously close to 0, the cluster is disordered. The spring constants K_N and K_ϕ, and the center of the biasing potential (N_c^0,Φ^0), are selected such that the statistics of neighboring windows overlap. Specifically, we perform 880 umbrella-sampling simulations for each scenario shown in Fig. 4 in the main text. For the binding strengths yielding square and stripe crystals, N_c^0 scans from 15 to 410 with an interval of 5, and Φ^0 scans from 0.0 to 1.0 with an interval of 0.1. For the

binding strengths yielding the honeycomb crystal, N_c^0 scans from 15 to 210 with an interval of 5 and Φ^0 scans from 0.0 to 1.0 with an interval of 0.05. K_N is chosen to be 0.125 k_BT for all scenarios. For the square case, K_Φ is 500 k_BT for simulations with $N_c^0 < 200$ and 1000 kT for simulations with $N_c^0 > 200$. K_Φ is 1000 k_BT for the stripe case and 3000 k_BT for the honeycomb case. Each umbrella-sampling simulation runs for 2.5×10^7 cycles to guarantee the system reaches equilibrium.

Although Φ does not explicitly distinguish between different compositional orders, we confirm from simulation snapshots that the system is biased between intended crystal structures. Fig. S7 shows the end-state snapshots of several umbrella-sampling simulations under different binding strengths. In each simulation, N_c and Φ of the biggest crystal in the simulation box are sampled.

Based on the statistics collected and the known biasing potential, we compute the local free energy landscape around the center of the biasing potential. We stitch together local free energy landscapes using the Weighted Histogram Analysis Method (WHAM) (4) to obtain the global free energy landscape with respect to N_c and Φ. We compute the free energy landscape based on the statistics collected from consecutive windows of 5×10^6 cycles from 1.5×10^7 to 2.5×10^7 cycles. The results are consistent with the exception of a few points near the edge of the free energy map, probably due to the lack of statistics. We fit the WHAM results to a fifth-order polynomial surface to fill in any gaps where the order parameter Φ is not well defined ($N_c < 5$). The coefficient of determination R^2 is above 0.995 for all three scenarios.

Ostwald's Step Rule. In the main text, we show that the two-step transition observed in our binary system follows one formulation of Ostwald's step rule: The phase that nucleates has lower free energy at small sizes, whereas the second phase has lower free energy at large sizes. However, the behavior that we observe does not necessary agree with an alternative formulation of Ostwald's step rule given by Stranski and Totomanow (5), which states that the phase that nucleates first is the phase that has the lowest free-energy barrier of formation, rather than the phase that has the lower free energy (6).

In our system, we hypothesize that the phase that forms first could have a higher free-energy barrier than the subsequent, stable phase for some specific combinations of binding free energies. Fig. S8a shows the free-energy landscape with respect to cluster size N_c and order parameter Φ for an AB binding free energy of 6.9 k_BT and a BB binding free energy of 2.2 k_BT. The stable phase at this combination of interaction strengths has a mixed composition of stripe and honeycomb patterns. The shaded area in Fig. S8a shows the distribution of paths followed by 200 independent unbiased Monte Carlo trajectories, which indicates again a two-step transition with a transition size of roughly 50 particles. Fig. S8b shows the free energy curves for the two dominant lattice structures. Here we see that the checkerboard lattice has the lower free energy before transition, yet a larger free-energy barrier compared with the stable lattice structure. This particular example suggests that our system might not satisfy the alternative statement of Ostwald's step rule since the metastable phase does not necessarily have a lower free-energy barrier than the stable crystal phase.

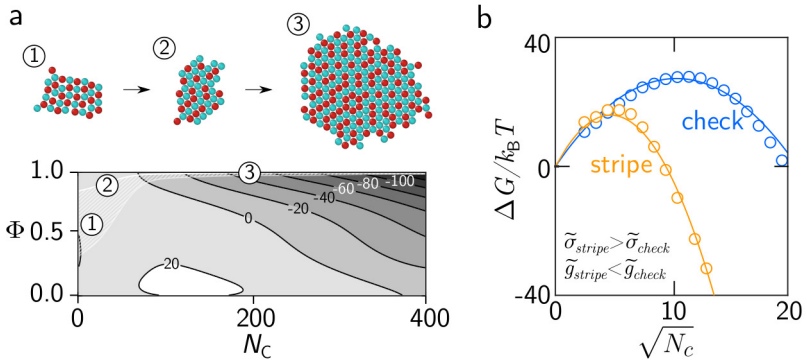

Fig. S8. (a) Free-energy landscape with respect to the crystal size N_c and the order parameter Φ. The white shaded region encloses 68 % of the pathways from 200 independent unbiased Monte Carlo simulations. Images show snapshots from unbiased simulations at different crystal sizes N_c. The contours show the free energy in k_BT. (b) Gibbs free energy G versus crystal size N_c for the free-energy landscape in (a). Blue circles and lines correspond to the checkerboard crystal; orange circles and lines correspond to the stripe crystal. The binding free energies are $E_{AA} = 0$, $E_{BB} = 2.2\ k_BT$, and $E_{AB} = 6.9\ k_BT$.

Transition Dynamics. Although it is possible to infer dynamics from Monte Carlo simulations in some cases, we have employed molecular dynamics simulations to investigate the kinetics and the mechanism of the checkerboard-stripe transition with fewer assumptions. Specifically, we use the HOOMD package (7), with the Brownian dynamics algorithm, and set the physical parameters to match our experiments: The particle diameter is 619 nm, the temperature is 60 °C, the dynamic viscosity is 8.9×10^{-4} Pa·s, and the density of the particles is 1.05 g/cm^3. We confirm that the single-particle dynamics of our MD simulations are accurate by measuring the diffusion coefficient of a single particle from its mean-squared displacement as a function of lag time. The diffusion coefficient that we find in simulations is 1.01 μm^2/s, while the theoretical prediction given by Einstein-Stokes equation is 0.97 μm^2/s. We point out that the diffusion coefficient that we measure in experiment is 0.39 μm^2/s, which is about 40 % of the theoretical prediction. This difference is most likely because of hydrodynamic interaction between the particles and their confining walls, which hinders diffusion.

We analyze the evolution of the local order within a single crystal during the checkerboard-stripe transition. We initialize our HOOMD simulations with a square lattice configuration from one of our unbiased MC simulations, which has an initial size close to the transition size. We then let the system evolve for 100 seconds. Fig. S9 shows how the local order changes during the checkerboard-stripe transition of a representative trajectory at $E_{BB} = 1.6\ k_{\mathrm{B}}T, E_{AB} = 7.0\ k_{\mathrm{B}}T$. Particles are color-coded by their species in the first row and color-coded by their local symmetry in the second row. A particle is considered to have hexagonal local symmetry if the absolute value of its bond orientation order parameter ψ_6 is above 0.9.

The transition that we find is reminiscent of a diffusionless solid-solid phase transition, in contrast to diffusive gas-solid or gas-liquid nucleation. At the very beginning of the transition, hexagonal domains appear stochastically within the cluster due to thermal fluctuations (Fig. S9a–d). These initial hexagonal domains exhibit some stripe order, as highlighted in Fig. S9b, yet are small and transient. Interestingly, we find that some of these transient hexagonal domains are often highly anisotropic, as highlighted in Fig. S9c: Long rows of particles spanning the entire crystal become close-packed and exhibit hexagonal order. Indeed we find that the formation of these domains is a regular occurrence (see Fig. S9f–g as well), with the long axis of the anisotropic domains always pointing along rows of atoms with alternating composition: $ABABABAB$. This alternating composition is due to the symmetry of the parent checkerboard phase. Such highly anisotropic regions are observed in other studies of solid-solid transitions (8, 9), but differ from diffusive, nucleation processes (10–12), where the initial nuclei are roughly isotropic. As the transition proceeds, the transient hexagonal domains merge to form larger hexagonal domains. Eventually, the hexagonal domain occupies the entire crystal. Fig. S9h shows the fraction of hexagonal particles in the cluster as a function of lag time, showing that the transition looks more like a biased random walk than nucleation and growth.

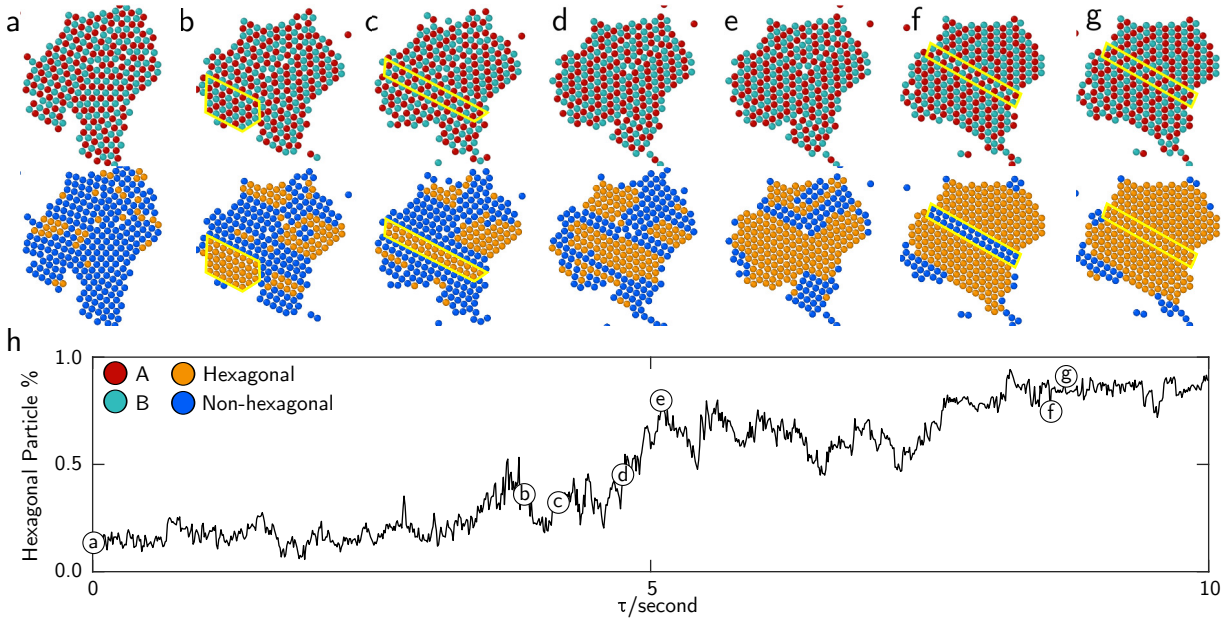

Fig. S9. A representative molecular dynamics simulation trajectory showing the evolution of local order during the checkerboard-stripe transition. (a–g) In the first row of snapshots, particles are color-coded by their species in red and cyan. In the second row of snapshots, particles are color-coded by whether their local order is hexagonal (orange) or square (blue). (h) The plot shows the fraction of hexagonally packed particles in the cluster as a function of lag time. Binding strengths: $E_{BB} = 1.6\ k_{\mathrm{B}}T, E_{AB} = 7.0\ k_{\mathrm{B}}T$

Both experiments and simulations show that parallel close-packed rows are created by coherent sliding of neighboring rows of particles. Fig. S10a shows bright-field micrographs of a single crystal formed at $\alpha = 0.3$ as a function of time. The two central rows undergo coherent sliding, as indicated by the white arrows, which show the relative orientation of neighboring particles. Fig. S10b shows similar snapshots from a HOOMD simulation at $E_{BB} = 1.6\ k_{\mathrm{B}}T, E_{AB} = 7.0\ k_{\mathrm{B}}T$. We take the B particle at the center of the frame to be a reference particle. A pair of white arrows again indicates the relative orientation between neighbors. Along the transition, we track the displacement ΔX, which we define as the projection of the orientation vector on the horizontal reference vector (Fig. S10c). D is the particle diameter. Fig. S10b shows the sliding displacement ΔX as a function of time for the corresponding snapshots. We see that one row of particles slides a full particle diameter and then returns to its initial configuration.

The sliding motion between neighboring rows is achieved by breaking 'like' bonds while preserving 'unlike' bonds. We analyze five independent simulation trajectories that exhibit multiple sliding transitions and characterize the probability density function of the shear displacement (Fig. S10c). We see two dominant peaks corresponding to the states in which the two rows are closely-packed, with some finite probability density between them. This probability density function corresponds to a free-energy landscape with two narrow minima separated by a roughly flat line, as expected for local rearrangements between particles interacting via short-range potentials (13). In contrast, we do not observe any probability density outside of $\pm D/2$, indicating that the sliding motion is constrained to a total displacement of one particle diameter. In other words, two rows cannot slide completely past one another. We hypothesize that the 'unlike' bonds prevent further sliding, since undergoing

larger displacements would require breaking 'unlike' bonds in addition to 'like' bonds. Interestingly, we point out that it would be possible for a checkerboard lattice to transform completely into a stripe lattice using only this sliding transition, with rows stochastically undergoing displacements of $\pm D/2$.

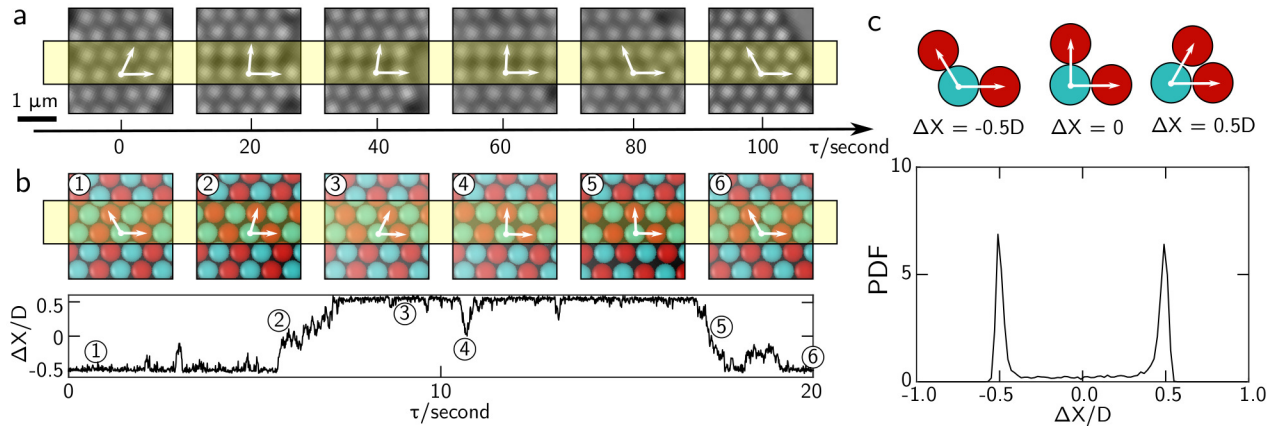

Fig. S10. Representative experimental and simulation trajectories showing sliding motion between neighboring rows of particles at weak 'like'-binding strengths. (a) Bright-field images at α = 0.3 show sliding motion between two neighboring rows of particles. Locations of sliding are highlighted in yellow. White arrows indicate the fixed orientation of the reference axis and the changing orientation of a bond between two neighboring particles in different rows. (b) The displacement as a function of lag time for a molecular dynamics simulation trajectory at $E_{BB} = 0.0$, $E_{AB} = 7.0\ k_{\mathrm{B}}T$, along with snapshots. (c) The probability density function of sliding displacements. The statistics are collected from 5 independent molecular dynamics trajectories, each lasting for twenty seconds.

The coherent sliding transition provides another way to conceptualize the relative stability of the stripe and checkerboard lattices above a given transition size: The stripe lattice is stabilized by a threshold number of 'like' bonds that form between neighboring rows. If the number of 'like' bonds between two rows is small, the sliding motion can convert stripe to checkerboard. However, if the number of 'like' bonds is prohibitively large, this motion will be suppressed, as it requires breaking one 'like' bond per particle. Thus the number of 'like' bonds is proportional to the length of the stripe. Following this train of thought, we can estimate a transition length scale by equating the Boltzmann weight of the checkerboard (open) and stripe (closed) states:

$$\int_{\Omega_{\mathrm{close}}} \exp\left(-\frac{NU_{\mathrm{AB}} + \frac{N}{2}U_{\mathrm{BB}}}{k_{\mathrm{B}}T}\right)d\Omega' = \int_{\Omega_{\mathrm{non\text{-}close}}} \exp\left(-\frac{NU_{\mathrm{AB}}}{k_{\mathrm{B}}T}\right)d\Omega', \qquad [5]$$

where Ω represents configurations that correspond to open or closed states, U_{ij} is the pair potential between particle species i and j, and N is the number of particles per row. Evaluating Equation 5 for $E_{BB} = 1.6\ k_{\mathrm{B}}T$ and $E_{AB} = 7.0\ k_{\mathrm{B}}T$—the conditions of Fig. 5b—we find a transition length scale of roughly 12 particles. Above this length scale, we expect the sliding transition to be disfavored and the stripe phase to predominate. Interestingly, the transition size that we find via this method is very close to the crystal size at which the checkerboard and stripe free-energy curves intersect (Fig. 5b), supporting this idea.

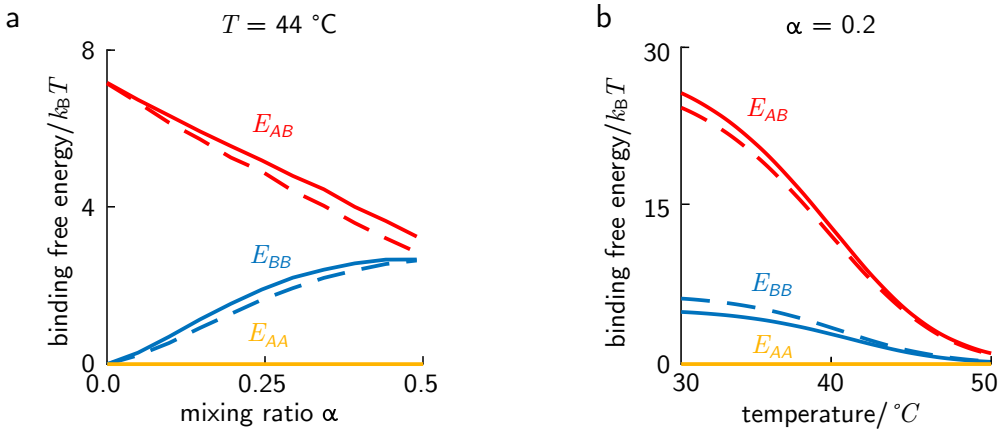

Fig. S11. Binding strengths as a function of mixing ratio α and temperature T. (a) *A-A*, *B-B* and *A-B* binding free energies as functions of mixing ratio α at a fixed temperature 44 °C. E_{BB} increases as α increases from 0 to 0.5. E_{AB} decreases monotonically as α increases. (b) Binding free energies as a function of temperature at fixed mixing ratio $\alpha = 0.2$. E_{AA} is always zero. E_{BB} and E_{AB} decreases monotonically as temperature increases. Dashed curves show predictions assuming that the relative grafting densities of *S* and *S** are directly proportional to the concentrations added; solid curves show predictions assuming that the relative grafting densities are off by a factor of 0.8, consistent with our experimental measurements.

Binding Strength Estimation. We use a mean-field model to estimate the binding free energies between our DNA-coated particles in the experiment. We assume the DNA reaches local chemical equilibrium in the interaction volume between neighboring particles in close contact. As described in Ref (3), the free energy difference between the unbound state and bound state is given by

$$\frac{\Delta F}{k_{\mathrm{B}}T} = \ln(P_{\mathrm{unbound}}) = N\ln(1-p) \quad [6]$$

where P_{unbound} is the probability that the particles are unbound and p is the probability that a single bridge is formed. N is the maximum number of bridges that can form.

We estimate N from experimental measurements of the melting temperatures T_m of a binary mixture contain A and B particles, as well as a unary mixture containing only B particles. More specifically, we assume that the average binding free energy at melting is roughly 5 $k_{\mathrm{B}}T$ and then fit a single value of N to 6 measurements of the melting temperature. The measured values of T_m depend on the mixing ratio α: T_m of the binary mixture decreases from 43 °C to 41 °C, while T_m of the unary mixture increases from 40 °C to 41°C, as α increases from 0.3 to 0.5. After finding a reasonable estimate for N, we calculate the relative binding free energies between like and unlike particles.

Fig. S11 shows example predictions of the binding free energies for various mixing ratios α and temperatures T. At fixed temperature, the A-B binding free energy decreases linearly as the mixing ratio α increases because the total number of bridges decreases as α increases (Fig. S11a). For a similar reason, the B-B binding free energy increases and reaches maximum at $\alpha = 0.5$. Fig. S11b shows that the binding free energies E_{BB} and E_{AB} decrease as temperature increases at fixed mixing ratio α. The monotonic decrease in the binding free energies comes from the fact that the binding affinities between complementary DNA molecules decrease as temperature increases, which causes the probability to form a single bridge to decrease as temperature increases.

Two-step Transitions and Classical Nucleation Theory. We analyze and interpret our free-energy landscapes within the framework of classical nucleation theory. Assuming our 2D crystals have circular shapes, we derive an expression for the change in Gibbs free energy between gas and crystal

$$\Delta G = \Delta g N_{\mathrm{bulk}} + \sigma N_{\mathrm{surface}} = \Delta g N_c + 2\sigma\gamma\sqrt{\frac{\pi N_c}{\rho}} = \widetilde{g}N_c + \widetilde{\sigma}\sqrt{N_c} \quad [7]$$

where Δg is the bulk free energy difference per particle, σ is the surface free energy per particle, N_{bulk} is the number of particles in the crystal, and N_{surface} is the number of particles at the surface of the crystal. N_{surface} is proportional to $\sqrt{N_{\mathrm{bulk}}}$. We define γ to be the line number density of the crystal surface and ρ to be the area number density of the crystal bulk. For the square symmetry, $\gamma = 1/D$ and $\rho = 1/D^2$; for the hexagonal symmetry, $\gamma = 1/D$ and $\rho = 2/\sqrt{3}D^2$. D is the particle diameter. We define an effective bulk free energy density $\widetilde{g}$ and an effective surface free energy density $\widetilde{\sigma}$, as shown in Eq. 7.

We fit the free energy as a function of cluster size to get the following values of the effective bulk free energy densities and surface free energies of different crystal symmetries (Fig. 5a–c). The subscripts indicate the corresponding lattice structures.

Binding Energy/$k_{\mathrm{B}}T$	$\widetilde{g}_{\mathrm{stripe}}/k_{\mathrm{B}}T$	$\widetilde{g}_{\mathrm{check}}/k_{\mathrm{B}}T$	$\widetilde{\sigma}_{\mathrm{stripe}}/k_{\mathrm{B}}T$	$\widetilde{\sigma}_{\mathrm{check}}/k_{\mathrm{B}}T$
$E_{BB} = 0.0, E_{AB} = 7.0$	-0.2	-0.2	5.1	4.3
$E_{BB} = 1.6, E_{AB} = 7.0$	-0.4	-0.3	6.2	4.8
Binding Energy/$k_{\mathrm{B}}T$	$\widetilde{g}_{\mathrm{honey}}/k_{\mathrm{B}}T$	$\widetilde{g}_{\mathrm{check}}/k_{\mathrm{B}}T$	$\widetilde{\sigma}_{\mathrm{honey}}/k_{\mathrm{B}}T$	$\widetilde{\sigma}_{\mathrm{check}}/k_{\mathrm{B}}T$
$E_{BB} = 3.5, E_{AB} = 6.3$	-1.0	0.5	8.2	5.2

Table S1. Estimates of the effective bulk and surface free energies.

The two-step crystallization pathway can be rationalized by considering the contributions to the bulk free energy and surface free energy. At finite temperature T, when $E_{BB} = 0$, $|\widetilde{g}_{\mathrm{stripe}}| \approx |\widetilde{g}_{\mathrm{check}}|$, $\widetilde{\sigma}_{\mathrm{stripe}} > \widetilde{\sigma}_{\mathrm{check}}$. As E_{BB} increases, $|\widetilde{g}_{\mathrm{stripe}}|$ and $\widetilde{\sigma}_{\mathrm{stripe}}$ increase owing to an increase in the binding free energy. When E_{BB} exceeds a certain limit, $|\widetilde{g}_{\mathrm{stripe}}|$ becomes significantly greater than $|\widetilde{g}_{\mathrm{check}}|$ and $\widetilde{\sigma}_{\mathrm{stripe}}$ remains greater than $\widetilde{\sigma}_{\mathrm{check}}$. As a result, the checkerboard lattice has lower free energy at small sizes, while the stripe lattice has a lower free energy at large sizes, leading to the two-step transition. Defining the transition size as the intersection point between two free energy curves yields a transition size N_t of

$$N_t = \left(\frac{\widetilde{\sigma}_{\mathrm{stripe}} - \widetilde{\sigma}_{\mathrm{check}}}{|\widetilde{g}_{\mathrm{stripe}}| - |\widetilde{g}_{\mathrm{check}}|}\right)^2. \quad [8]$$

Therefore, when E_{BB} decreases to approach the phase boundary between square and stripe crystals, $|\widetilde{g}_{\mathrm{stripe}}| - |\widetilde{g}_{\mathrm{check}}|$ approaches zero from positive side and the transition size N_t approaches infinity.

We estimate the effective surface free energy per particle using a similar bond-counting argument described in the main text. In general, the surface free energy is equivalent to the work needed to create two interfaces by splitting a bulk crystal along a given lattice vector. We consider only the lattice vectors that yield the lowest surface free energies for our three crystal lattices: checkerboard, stripe, and honeycomb (Fig. S12). For the checkerboard lattice, each particle loses one 'unlike' bond. For the stripe lattice, each particle loses one 'like' bond and one 'unlike' bond. For the honeycomb lattice, each B particle loses two

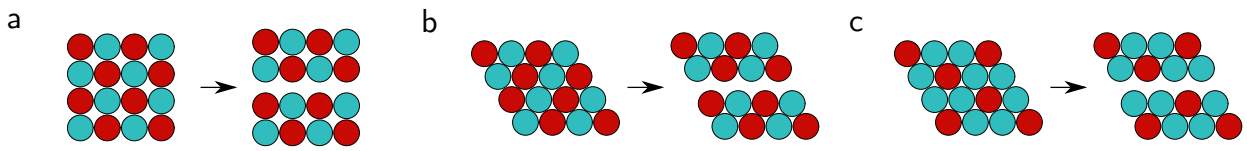

Fig. S12. Schematic diagram that shows the splitting of a bulk crystal to create two interfaces. (a) Splitting of the checkerboard lattice along $ABAB$. (b) Splitting of the stripe lattice along $ABAB$. (c) Splitting of the honeycomb lattice along $ABBABB$.

'unlike' bonds and each A particle loses one 'like' bond and one 'unlike' bond. The stoichiometry of A:B in the honeycomb lattice is 1:2.

We estimate the strength of each bond using the approach outlined in Ref (14), which calculates the free energy difference between bound and unbound states from a continuous potential according to:

$$F_{\text{bound}} - F_{\text{unbound}} = -\log\left[\frac{1}{\pi(\delta^2 + 2R\delta)}\int_R^{R+\delta}\exp\left(-\frac{U(r)}{k_B T}\right)2\pi r dr\right], \quad [9]$$

where R is the radius of the particle, r is the center-to-center distance between two particles, $U(r)$ is the pair interaction potential, and δ is the range of the attraction. The estimated values of the effective surface free energies are given in Table S2.

	$\widetilde{\sigma}_{\text{check}}/k_{\text{B}}T$		$\widetilde{\sigma}_{\text{stripe}}/k_{\text{B}}T$		$\widetilde{\sigma}_{\text{honey}}/k_{\text{B}}T$	
Binding Free Energy/$k_{\text{B}}T$	Landscape	Bond-counting	Landscape	Bond-counting	Landscape	Bond-counting
$E_{BB} = 0.0, E_{AB} = 7.0$	4.3	7.1	5.1	6.6	–	–
$E_{BB} = 1.6, E_{AB} = 7.0$	4.8	7.1	6.2	6.9	–	–
$E_{BB} = 3.5, E_{AB} = 6.3$	5.2	6.0	–	–	8.2	9.8

Table S2. Estimates of the effective surface free energies from bond counting.

Our bond-counting estimates of the effective surface free energies are of the same order of magnitude, yet generally larger than the values that we extract from the free-energy landscapes. We hypothesize that this discrepancy arises because we ignore entropy in our bond-counting estimate, which decreases the effective surface free energy $\widetilde{\sigma}$ since fluctuations of particles at the surface are less constrained than those of particles in the bulk of the crystal. Interestingly, we also find that our estimate of the surface free energy of the checkerboard lattice $\widetilde{\sigma}_{\text{check}}$ is greater than our estimate of the stripe lattice $\widetilde{\sigma}_{\text{stripe}}$ for strong 'unlike' attraction and weak 'like' attraction, which disagrees with our results from the free-energy landscapes (Table S2). This inconsistency is again most likely due to the fact that we ignore entropy in our bond-counting approach. Therefore we hypothesize that the entropy of checkerboard lattice contributes more strongly to the effective surface free energy $\widetilde{\sigma}$ than in the stripe lattice.

Movie S1. Crystallization process under bright-field microscope for the binary system with $\alpha = 0.0$

Movie S2. Crystallization process under bright-field microscope for the binary system with $\alpha = 0.3$

Movie S3. Crystallization process under bright-field microscope for the binary system with $\alpha = 0.5$

Movie S4. Grand Canonical Monte Carlo trajectory under the binding strengths $E_{BB} = 0.0, E_{AB} = 7.1\ k_{\mathbf{B}}T$

Movie S5. Grand Canonical Monte Carlo trajectory under the binding strengths $E_{BB} = 1.6, E_{AB} = 7.1\ k_{\mathbf{B}}T$

Movie S6. Grand Canonical Monte Carlo trajectory under the binding strengths $E_{BB} = 3.5, E_{AB} = 6.5\ k_{\mathbf{B}}T$

References

1. JS Oh, Y Wang, DJ Pine, GR Yi, High-Density PEO-b-DNA Brushes on Polymer Particles for Colloidal Superstructures. *Chem. Mater.* **27**, 8337–8344 (2015).
2. D Blair, E Dufresne, http://site.physics.georgetown.edu/matlab/ (2005).
3. WB Rogers, JC Crocker, Direct measurements of DNA-mediated colloidal interactions and their quantitative modeling. *Proc. Natl. Acad. Sci.* **108**, 15687–15692 (2011).
4. S Kumar, JM Rosenberg, D Bouzida, RH Swendsen, PA Kollman, THE weighted histogram analysis method for free-energy calculations on biomolecules. I. The method. *J. Comput. Chem.* **13**, 1011–1021 (1992).
5. IN Stranski, D Totomanow, Keimbildungsgeschwindigkeit und ostwaldsche stufenregel. *Zeitschrift für Physikalische Chemie* **163A**, 399–408 (1933).
6. PRt Wolde, D Frenkel, Homogeneous nucleation and the Ostwald step rule. *Phys. Chem. Chem. Phys.* **1**, 2191–2196 (1999).
7. JA Anderson, J Glaser, SC Glotzer, HOOMD-blue: A Python package for high-performance molecular dynamics and hard particle Monte Carlo simulations. *Comput. Mater. Sci.* **173**, 109363 (2020).
8. CX Du, Gv Anders, RS Newman, SC Glotzer, Shape-driven solid–solid transitions in colloids. *Proc. Natl. Acad. Sci.* **114**, E3892–E3899 (2017) Publisher: National Academy of Sciences Section: PNAS Plus.
9. J Meiser, HM Urbassek, Martensitic transformation of pure iron at a grain boundary: Atomistic evidence for a two-step Kurdjumov-Sachs–Pitsch pathway. *AIP Adv.* **6**, 085017 (2016) Publisher: American Institute of Physics.
10. Y Wang, et al., Crystallization of DNA-coated colloids. *Nat. Commun.* **6**, 1–8 (2015).
11. JR Savage, AD Dinsmore, Experimental Evidence for Two-Step Nucleation in Colloidal Crystallization. *Phys. Rev. Lett.* **102**, 198302 (2009).
12. TH Zhang, XY Liu, How Does a Transient Amorphous Precursor Template Crystallization. *J. Am. Chem. Soc.* **129**, 13520–13526 (2007).
13. M Holmes-Cerfon, SJ Gortler, MP Brenner, A geometrical approach to computing free-energy landscapes from short-ranged potentials. *Proc. Natl. Acad. Sci.* **110**, E5–E14 (2013).
14. N Ben-Tal, B Honig, CK Bagdassarian, A Ben-Shaul, Association entropy in adsorption processes. *Biophys. J.* **79**, 1180–1187 (2000).